

# Lawrence Berkeley National Laboratory

## LBL Publications

### Title

Editors' Choice—Ionomer Side Chain Length and Equivalent Weight Impact on High Current Density Transport Resistances in PEMFC Cathodes

### Permalink

<https://escholarship.org/uc/item/26b8q2gw>

### Journal

Journal of The Electrochemical Society, 168(2)

### ISSN

0013-4651

### Authors

Ramaswamy, Nagappan  
Kumaraguru  
Koestner, Roland  
[et al.](#)

### Publication Date

2021-02-01

### DOI

10.1149/1945-7111/abe5eb


Peer reviewed

**OPEN ACCESS**

## Editors' Choice—Ionomer Side Chain Length and Equivalent Weight Impact on High Current Density Transport Resistances in PEMFC Cathodes

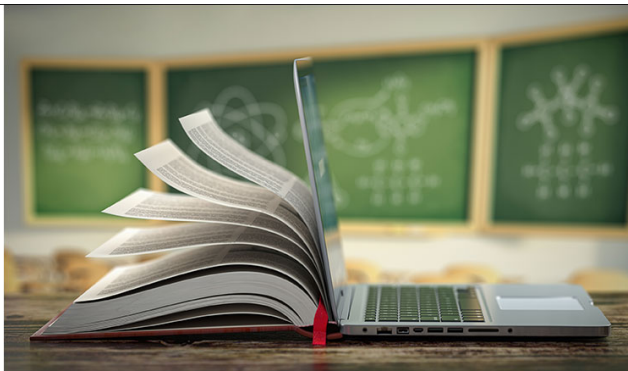
To cite this article: Nagappan Ramaswamy *et al* 2021 *J. Electrochem. Soc.* **168** 024518

View the [article online](#) for updates and enhancements.

 The Electrochemical Society  
Advancing solid state & electrochemical science & technology  
2021 Virtual Education




**Fundamentals of Electrochemistry:**  
Basic Theory and Kinetic Methods  
Instructed by: **Dr. James Noël**  
Sun, Sept 19 & Mon, Sept 20 at 12h–15h ET

Register early and save!





## Editors' Choice—Ionomer Side Chain Length and Equivalent Weight Impact on High Current Density Transport Resistances in PEMFC Cathodes

Nagappan Ramaswamy,<sup>1,\*</sup>  Swami Kumaraguru,<sup>1</sup> Roland Koestner,<sup>1</sup> Timothy Fuller,<sup>1</sup> Wenbin Gu,<sup>1</sup> Nancy Kariuki,<sup>2</sup>  Deborah Myers,<sup>2,\*</sup>  Peter J. Dudenas,<sup>3</sup> and Ahmet Kusoglu<sup>3,\*</sup> 

<sup>1</sup>Global Fuel Cell Business, General Motors Company, Pontiac, Michigan 48340, United States of America

<sup>2</sup>Chemical Sciences and Engineering Division, Argonne National Laboratory, Argonne, Illinois 60439, United States of America

<sup>3</sup>Energy Conversion Group, Lawrence Berkeley National Laboratory (LBNL), Berkeley, California, 94720, United States of America

Cell voltage at high current densities (HCD) of an operating proton-exchange membrane fuel cell (PEMFC) suffers from losses due to the local-O<sub>2</sub> and bulk-H<sup>+</sup> transport resistances in the cathode catalyst layer (CCL). Particularly, the interaction of perfluorosulfonic acid (PFSA) ionomer with the carbon supported platinum catalyst plays a critical role in controlling reactant transport to the active site. In this study, we perform a systematic analysis of the side chain length and equivalent weight (EW) of PFSA ionomers on the CCL transport resistances. Ex situ measurements were carried out to quantify the ionomer characteristics such as the molecular weight, proton conductivity and water uptake. Nanomorphology of ionomers cast as 60–120 nm thin-films is characterized using grazing-incidence X-ray scattering. In situ fuel cell electrochemical diagnostic measurements were carried out to quantify the reactant (H<sup>+</sup>/O<sub>2</sub>) transport properties of the CCL. Ionomer EW was found to play a major role with decreasing EW yielding higher proton conductivity and water uptake that led to lower bulk-H<sup>+</sup> and local-O<sub>2</sub> transport resistances in the CCL. Finally, a 1D-semi-empirical performance model has been developed to quantify the impact of ionomer EW on cell voltage loss factors.

© 2021 The Author(s). Published on behalf of The Electrochemical Society by IOP Publishing Limited. This is an open access article distributed under the terms of the Creative Commons Attribution 4.0 License (CC BY, <http://creativecommons.org/licenses/by/4.0/>), which permits unrestricted reuse of the work in any medium, provided the original work is properly cited. [DOI: 10.1149/1945-7111/abe5eb]



Manuscript submitted January 15, 2021; revised manuscript received February 9, 2021. Published February 22, 2021.

PEMFC cathode electrodes are composed of carbon supported Pt nanoparticle-based catalyst materials (Pt/C) dispersed along with PFSA ionomeric binder for Oxygen Reduction Reaction (ORR). The high cost associated with Pt/C catalysts is a major barrier towards the commercialization of PEMFC devices for automotive applications. Development of well-optimized electrode structures with highly active Pt-alloy/C catalysts has enabled cathode loadings of ~0.2 mg<sub>Pt</sub> cm<sup>-2</sup>. While this represents a major improvement, widespread commercialization of PEMFCs require a further decrease in Pt usage to ≤0.1 mg<sub>Pt</sub> cm<sup>-2</sup>.<sup>1,2</sup> Studies in the past decade have identified the presence of reactant (H<sup>+</sup>/O<sub>2</sub>) transport resistances in the CCL that scales inversely with Pt loading as a major barrier towards decreasing Pt content any further.<sup>3–6</sup> Specifically, there are two resistances in the CCL with respect to O<sub>2</sub> transport corresponding to the i) presence of micro/mesopores in the Pt/C agglomerates, and ii) ionomer thin film surrounding the Pt/C agglomerates.<sup>1,6,7</sup>

The former resistance arises since O<sub>2</sub> is transported within the tortuous pore structure of the Pt/C agglomerates to reach the active site. High surface area carbon (HSC) supports used for the deposition of Pt nanoparticles are highly porous materials featuring primary pores characterized micropores (<2 nm) and small mesopores (2 to 5 nm) in its primary particles.<sup>8</sup> The pores between these primary particles are called the secondary pores characterized by the larger mesopores (5 to 50 nm) and macropores (>50 nm) that are functionally needed for gas/water transport. Pt nanoparticles are deposited both inside and outside these pores with some studies quantifying as much as 50%–80% of Pt inside primary particles.<sup>9,10</sup> Our recent studies have shown that the experimentally measured local-O<sub>2</sub> and bulk-H<sup>+</sup> transport resistances are linearly correlated to the micropore volume and macropore volume of the HSC supports, respectively.<sup>11</sup> Further, porous carbons with preferred mesopore

openings of 4–7 nm could give catalyst layers with a high ORR kinetic activity since it prevents the direct contact between Pt and PFSA ionomer.<sup>12</sup> This indicates that carbon supports that feature minimal micro- and macro-pore volume along with an appreciable content of mesopore regions (in the range of ~5 nm) would deliver catalyst layers with high ORR kinetic activities and low local-O<sub>2</sub>/bulk-H<sup>+</sup> transport resistances, and hence an improved performance across all polarization regions.

The presence of ionomer thin film surrounding the Pt/C agglomerates also leads to an O<sub>2</sub> transport resistance in the CCL.<sup>7</sup> PFSA ionomer is a random copolymer of semicrystalline polytetrafluoroethylene and perfluorovinyl ether sidechain with pendant sulfonic acid ion exchange groups for H<sup>+</sup> transport. The primary role of PFSA ionomer in the cathode is to extend the three-phase boundary thereby enabling proton transport across the catalyst layer while also acting as a physical binder.<sup>13–15</sup> An optimal ionomer content is required in the catalyst layer—too much ionomer leads to blockage of secondary pores for bulk gas transport whereas sub-optimal levels lead to high H<sup>+</sup> transport resistance and poor catalyst utilization. While the PFSA ionomer plays a critical functional role in the CCL by providing H<sup>+</sup> transport pathways, a major drawback arises due to conflicting requirements for use in CCL and membranes. Ionomers designed for use in membranes with a lower gas permeability requirement is largely used in CCL. This coupled with the adsorption of sulfonate anions that poisons the Pt catalyst surface leading to a decrease in both ORR activity and O<sub>2</sub> permeability through the ionomer thin film covering the Pt/C agglomerates.<sup>7,16–18</sup>

Understanding the interfacial structure and adsorption characteristics of the PFSA ionomer on Pt surfaces has been the subject of various investigations.<sup>17</sup> Negatively charged sulfonate anion in the ionomer is known to adsorb on the Pt surface via a reversible, potential-dependent specific adsorption process between 0.1 V and 0.8 V followed by a gradual desorption at higher potentials where Pt-oxide is formed.<sup>18–24</sup> Besides the direct sulfonate adsorption, several spectroscopic studies have also observed potential-dependent co-adsorption of other functional groups in the PFSA ionomer such as

\*Electrochemical Society Member.

<sup>z</sup>E-mail: [Nagappan.Ramaswamy@gm.com](mailto:Nagappan.Ramaswamy@gm.com)

the ether linkages and  $-\text{CF}_3$  moieties on Pt thereby amplifying the impact of surface contamination.<sup>19,25–27</sup>

Pt-ionomer interactions cause ionomer structural changes and ionomer film densification adjacent to Pt resulting in a loss of effective surface area for ORR and/or a decrease in  $\text{O}_2$  permeability.<sup>7,24,28,29</sup> The ionomer thin film in the catalyst layer (roughly a few nm thick) is spatially confined due to the Pt-side chain interactions which causes its physical and chemical properties to deviate from that of the bulk membrane (few  $\mu\text{m}$  thick).<sup>1,30</sup> Ionomer thin film is observed to suffer from a decrease of water uptake, loss in phase separation, stiffening of ionomer backbone compared to bulk membrane.<sup>31–33</sup> Sulfonate adsorption and measured local- $\text{O}_2$  transport resistances are observed to be strongly dependent on the ionomer water content with sub-saturated conditions leading to stronger, earlier onset of sulfonate adsorption and higher local- $\text{O}_2$  transport resistances.<sup>29,34</sup> These deleterious effects cause a loss of mass activity (due to sulfonate poisoning of Pt) and a decrease in  $\text{O}_2$  permeability (dissolution and diffusion) through the ionomer thin film.

New operational strategies and novel ionomer materials have been developed to overcome this challenge. For instance, since sulfonate adsorption is a reversible process a voltage recovery operation is typically carried out at high RH ( $\geq 90\%$  RH) and/or low potentials ( $\leq 0.2$  V) during which the cell voltage losses are recovered.<sup>7,35</sup> From a materials point of view, several authors have reported the use of i) alternate side-chain structures/functional groups,<sup>25,36</sup> ii) ionomers with rigid backbone,<sup>7</sup> iii) ionomers with short-side chain (SSC) lengths,<sup>37,38</sup> iv) modified catalyst surface structures,<sup>39</sup> and v) catalyst ink solvents.<sup>40</sup> Kodama et al. reported minor improvements in ORR kinetic properties of Pt(111) single crystal using a novel ionomer consisting of two sulfonimide functional groups in the side chain with terminal perfluorobutane end group since sulfonimide adsorption on Pt is predicted to be weaker than sulfonate anions.<sup>36</sup> Ionomers with rigid backbone and short-side chain lengths have been reported to prevent sulfonate adsorption due to the restricted motion of side chains.<sup>7</sup> Several studies have looked at the role of ionomer EW and its properties on CCL layer to investigate  $\text{O}_2$  mass transport limitations. Early microelectrode investigations highlight the role of EW on  $\text{O}_2$  solubility and diffusivity in ionomer phase.<sup>41</sup> Recent studies have focused on reducing ionomer content in CCL with use of lower EW and subsequent larger pore volume for gas transport. For instance, optimal ionomer content in the CCL decreases from 32% for 1100EW to 25% for 800EW.<sup>38,42</sup> Low EW ionomers, due to their higher water uptake<sup>38,43</sup> and/or higher proton conductivity<sup>44</sup> enable substantial improvements in cell voltages particularly at higher operating temperatures ( $> 80$  °C) and sub-saturated RH conditions ( $\leq 90\%$  RH).<sup>37,38,42–46</sup> Some results also suggest that the low EW, SSC ionomer gets distributed on the catalyst surface more uniformly leading to a better catalyst utilization compared to a long side chain (LSC) ionomers that tend to form non-homogeneous films on catalyst surface.<sup>44,45</sup> Most studies in the literature using low EW, SSC ionomers in the CCL largely focus on the bulk transport properties such as the intermolecular  $\text{O}_2/\text{H}_2\text{O}$  transport through the secondary pores of the catalyst layer.

In the work reported here, we attempt to understand the impact of ionomer properties on the cathode kinetics, bulk- $\text{H}^+$  and specifically, the local- $\text{O}_2$  transport characteristics using in situ fuel cell electrochemical diagnostic methodologies. To this end, we choose PFSA ionomer side chain length and EW as two parameters of interest and systematically evaluate their impact on the CCL performance. Our studies indicate that the EW is the dominant property of the PFSA ionomer in such a way that its decrease leads to higher water uptake and hence, lower local- $\text{O}_2$  transport resistance in the CCL.

## Experimental

**Materials and membrane electrode assembly (MEA) fabrication.**—Commercially procured PtCo/HSC-a catalyst material with a

total metal loading of 30% by weight and Pt:Co atomic ratio of (3:1) was used here in consistency with our earlier work.<sup>11</sup> Eight different PFSA ionomers from three different suppliers were procured. Two LSC ionomers with EWs of 950 and 1100  $\text{g mmol}^{-1}$ , three mid side chain (MSC) ionomers with EWs of 725, 825, 1000  $\text{g mmol}^{-1}$  and three SSC ionomers with EWs of 720, 790, 870, 980  $\text{g mmol}^{-1}$  were used in this study. Ionomers are labelled to indicate their chain length and EW—for instance, the LSC ionomer with 950EW is labelled as LSC-950EW in this work. LSC-950EW ionomer corresponds to the commercially available DuPont Nafion® D2020 PFSA dispersion and is considered as the baseline ionomer in this work. All ionomers were procured as liquid dispersions except the MSC materials that were available only in their powder form. Cathode catalyst inks were made by dispersing the catalyst along with the appropriate amount of ionomer in n-propanol to water (3:1) solvent mixture followed by ball milling for 24 h. Cathode I/C in the ink for the ionomers of various EWs were normalized to the optimal sulfonic acid content of LSC-950EW ionomer at 0.9 I/C. For instance, sulfonic acid molality of LSC-950EW ionomer at 0.9 I/C is 28.4  $\text{mmol kg}^{-1}$ . I/C values for all the other ionomers were calculated to yield the same sulfonic acid molality of 28.4  $\text{mmol kg}^{-1}$ . This gave the following I/C values for each of the ionomers used in this study—1.04, 0.69, 0.78, 0.95, 0.68, 0.75, 0.82, 0.91 I/Cs for LSC-1100EW, MSC-725EW, MSC-825EW, MSC-1000EW, SSC-720EW, SSC-790EW, SSC-870EW, SSC-980EW ionomers. This enables a direct comparison of these ionomers with various EWs. Cathode inks were coated on decal substrates at various loadings from 0.05 to 0.2  $\text{mg}_{\text{Pt}} \text{cm}^{-2}$ . All anode catalyst layers were composed of 10% Pt/C catalyst, LSC-950EW ionomer at a fixed loading of 0.025  $\text{mg}_{\text{Pt}} \text{cm}^{-2}$  (anode catalyst layer I/C of 0.6 was used). MEAs with 5  $\text{cm}^2$  active area were fabricated via decal transfer of the anode and cathode catalyst layers on either side of an 18  $\mu\text{m}$  thick mechanically reinforced PFSA membrane. Roughly 230  $\mu\text{m}$  thick carbon fiber paper based gas diffusion layer (GDL) was used on both the anode and cathode sides.

**Physical characterizations of ionomers.**—As received ionomer materials were subjected to several characterizations to evaluate their physico-chemical properties such as molecular weight and intrinsic viscosity via size-exclusion chromatography (SEC), proton conductivity, water uptake/lambda parameter, and colloidal structure via small angle X-ray scattering. To perform SEC measurements, the ionomer dispersions were autoclaved in a Parr bomb at 230 °C for 6 h at a concentration of  $\sim 0.1$  wt% PFSA in 80:20 (w/w) n-propanol/water. Single phase solutions were obtained after autoclaving; aliquots were further diluted with N,N-dimethylformamide (DMF) and subsequently concentrated under nitrogen to give sample concentrations of  $\sim 1.5$   $\text{mg ml}^{-1}$ . The SEC eluent was formulated in DMF with 0.1 M  $\text{LiNO}_3$  at 45 °C. The column set comprised three Shodex KD-806M SDVB columns which were calibrated with 15 narrow-cut poly (methyl methacrylate) (PMMA) standards ranging from 680 to 1400000  $\text{g mol}^{-1}$ . The system had multiple detectors to measure differential refractive index (DRI), intrinsic viscosity, UV-visible absorption and light scattering elastically at 15 and 90 degrees.<sup>47,48</sup> In-plane proton conductivity of the ionomers was measured by coating them as 20  $\mu\text{m}$  membranes (typically, from a 10% ionomer dispersions in water/alcohol mixture) followed by measurement in a four-probe conductivity setup at 80 °C as a function of RH from 20% to 100%. Water uptake measurements were carried out on a known weight of a rectangular ionomer membrane sample of dimensions 5 cm by 1 cm by soaking it in boiling water (100 °C) for 1 h. After the soaking treatment, excess water was removed followed by measurements of changes in the three dimensions ( $x$ ,  $y$ ,  $z$ ) and gravimetric weight. Water content of the ionomer or the lambda parameter ( $\lambda$ ) defined as the number of water molecules per sulfonic acid ion exchange group ( $\text{H}_2\text{O}/\text{SO}_3\text{H}$ ) was calculated as  $(\text{weight gain} * 10)/(\text{M}_{\text{H}_2\text{O}} * \text{IEC})$  where IEC refers to ion exchange capacity of ionomer in  $\text{mmol g}^{-1}$  and  $\text{M}_{\text{H}_2\text{O}}$  is molar mass of water.

The X-ray scattering data were collected on a combined USAXS and pinSAXS instrument at beamline 9-ID-C at the Advanced Photon Source at Argonne National Laboratory. The X-ray beam was monochromatized via a pair of Si(220) crystals to an energy of 21 keV. The geometric size of the X-ray beam was  $0.4 \times 0.2$  mm. The ionomer solution samples at a concentration of 3% PFSA solids in n-propanol/water (3/1) solvent mixture were placed in 5 mm (ID) capillaries and were supported in a custom-made sample holder for the measurements. During data reduction, patterns collected on blank sample were subtracted from the patterns acquired for the samples.

For measurements to study the nanomorphology, ionomer solutions were prepared by dilution with n-propanol/water mixture (3/1 ratio) to achieve 3 wt.% of PFSA solids. Si substrate diced to  $1.5 \times 1.5$  cm was cleaned in subsequent rinses of acetone and IPA before being blow dried with  $N_2$ . Ionomer thin films were cast onto the Si substrates via spin coating at 3000 rpm for 60 s and then annealed at  $150^\circ\text{C}$  for 1 h. Humidified grazing-incidence small angle X-ray scattering (GISAXS) measurements were performed in situ at beamline 7.3.3 of the ALS at LBNL using a custom-built environmental chamber.<sup>49</sup> The X-ray energy was 10 keV ( $\lambda = 1.24 \text{ \AA}^{-1}$ ) with a monochromator energy resolution  $E/dE$  of 100, and the patterns were acquired with a Dectris Pilatus 2 M CCD area detector ( $172 \mu\text{m} \times 172 \mu\text{m}$  pixel size). GISAXS images were collected at grazing incidence angles ( $\alpha_i$ ) of  $0.14$ – $0.20^\circ$  with 5 s exposure. Samples were equilibrated at 95% RH for 45 min before collecting images. Extracted values in the manuscript are from analyzing through-plane sector cuts from the images collected at  $0.16^\circ$ . Data reduction was done using custom scripts written in Matlab.

**Electrochemical diagnostics.**—In situ characterizations of the CCLs to quantify kinetic activities, H-adsorption electrochemical surface area (ECSA), CO adsorption/stripping ECSA,  $H_2$ /air polarization curves, and  $H^+$ / $O_2$  transport resistances were carried out in a single-cell test fixture comprising of  $5 \text{ cm}^2$  active area MEA (0.5 mm lands/channels).<sup>3,11,12,50</sup> ORR activities were measured at 0.9 V using polarization curves obtained with pure  $H_2$  and  $O_2$  as the reactant gases in the anode and cathode, respectively. The relative humidity (RH) of the inlet gas was maintained at 100% with the cell temperature maintained at  $80^\circ\text{C}$  at an absolute outlet pressure of 150 kPa. The activity at 0.9 V was determined using the Tafel plot which is a semi-log plot of the Ohmic-resistance corrected cell voltage vs  $H_2$  gas crossover corrected current density.  $H_2$ /air polarization curves with high stoichiometric feed of the reactant gases were measured at various operating conditions with cell temperatures ranging from  $80$  to  $94^\circ\text{C}$ , RH values from 65 to 100%, and absolute outlet pressures of 150 to 250 kPa.

Local- $O_2$  transport resistance ( $R_{O_2\text{-local}}$ ) was calculated using the limiting current density measurements at low  $O_2$  partial pressures under operating conditions of  $80^\circ\text{C}$  and  $\sim 70\%$  RH under differential cell conditions (1000 sccm of  $H_2$  and 5000 sccm of  $O_2/N_2$  mixtures).<sup>3,11,12,39</sup>  $O_2$  limiting current densities were measured at potentials below 0.3 V at various  $O_2$  mole fractions (1% to 4%) as a function of outlet pressures (110 to 300 kPa<sub>abs</sub>).  $O_2$  limiting current densities measurements were carried out for each catalyst at three different cathode Pt loadings (0.05, 0.1, 0.2 mg<sub>Pt</sub> cm<sup>-2</sup>). The total  $O_2$  transport resistance of the cathode electrode consists of both the pressure-dependent and pressure-independent terms.  $R_{O_2\text{-local}}$  can be extracted from the pressure-independent portion of the resistance. The procedure to extract  $R_{O_2\text{-local}}$  is as follows.<sup>51,52</sup> First, the total  $O_2$  transport resistance at any given outlet pressure is calculated as the slope of the plot between the limiting current density and  $O_2$  mole fraction. The slope of the plot between total transport resistance and outlet pressure gives the pressure-dependent resistance whereas the intercept at zero total pressure yields pressure-independent resistance. Subsequently, the slope derived from a plot of pressure-independent transport resistance vs the inverse roughness factor of the catalyst layer (derived from the hydrogen-underpotential

deposition ( $H_{UPD}$ ) ECSA at various loadings) was measured as the experimentally determined  $R_{O_2\text{-local}}$  value.

Bulk proton transport resistance of the catalyst layer was measured using an electrochemical impedance spectra (EIS) methodology.<sup>50,53</sup> This involved the flow of  $H_2$  on the anode and  $N_2$  on the cathode at  $80^\circ\text{C}$  and various RH values from 20% to 122%. EIS measurement was carried out to quantify proton conduction resistance at a DC potential of 0.2 V with 0.15 mV amplitude from a frequency of 0.5 Hz to 20 kHz with twenty points per decade. EIS profile was fitted to a transmission line model from which the proton transport resistance in the membrane ( $R_{H^+, \text{membrane}}$ ) and the cathode catalyst layer ( $R_{H^+, \text{cathode}}$ ) were obtained. The effective proton transport resistance ( $R_{H^+}^{\text{eff}}$ ) in the cathode was then calculated by correcting the measured value according to the equation  $R_{H^+}^{\text{eff}} = R_{H^+, \text{cathode}} / (3 + \zeta)$ , where  $\zeta$  is a correction factor that accounts for the effect of catalyst utilization on the effective length for protons with the cathode to transport to the membrane.<sup>54</sup>

## Results and Discussion

PFSA is a phase-segregated, perfluorinated ionomeric material consisting of a fluorinated-carbon backbone composed of semicrystalline polytetrafluoroethylene (PTFE) with a fluoroether sidechains ending with a pendant sulfonic acid ion-exchange group. Generic chemical structure of PFSA is shown in Fig. 1 with the variable  $m$  representing the number of TFE repeat units in the backbone. PFSA is characterized by its EW value defined as the grams of dry ionomer per mole of sulfonic acid group in the acid ( $H^+$ ) form. The length of the side chain is defined by the structural parameters  $x$  and  $y$ . The commercially available DuPont Nafion<sup>®</sup> ionomer is characterized by a long side chain ( $x = 1$ ,  $y = 2$ ) with four carbon units and an EW value of  $950 \text{ g mmol}^{-1}$ . MSC ionomers are characterized by  $x = 0$  and  $y = 4$  and whereas the SSC ionomers are characterized by  $x = 0$  and  $y = 2$ . LSC ionomers consist of two ether linkages in its side chain whereas the MSC and SSC variants consist of only one ether linkage. The structural morphology of hydrated PFSA ionomer is typically described by the locally-flat interconnected water-domain network model.<sup>30</sup> According to this model, water-solvated ion-exchange groups form a hydrophilic phase distinct from the hydrophobic backbone, leading to nano-phase separation. This hydrophilic phase of this phase-separated network provides ion-transport pathways through which the proton transport occurs.<sup>30</sup>

EW of the ionomer is related to the number of TFE repeat units in the backbone via the equation,  $EW = 100m + MW_{SC}$  where  $MW_{SC}$  represents the molecular weight of the side chain. According to this equation, for a given EW shorter side chain lengths (or lower

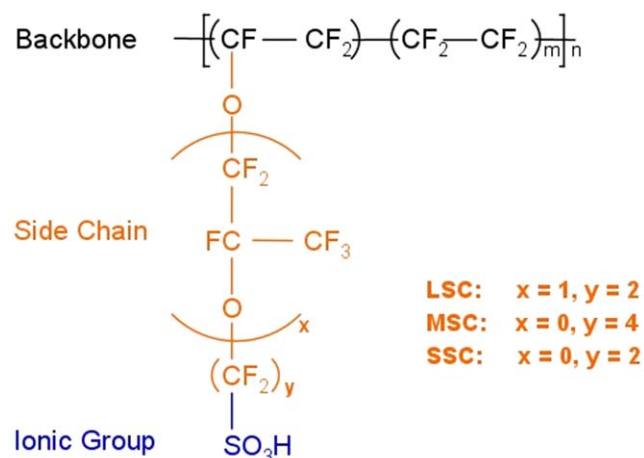


**Figure 1.** Schematic of the PFSA ionomer chemical structure.

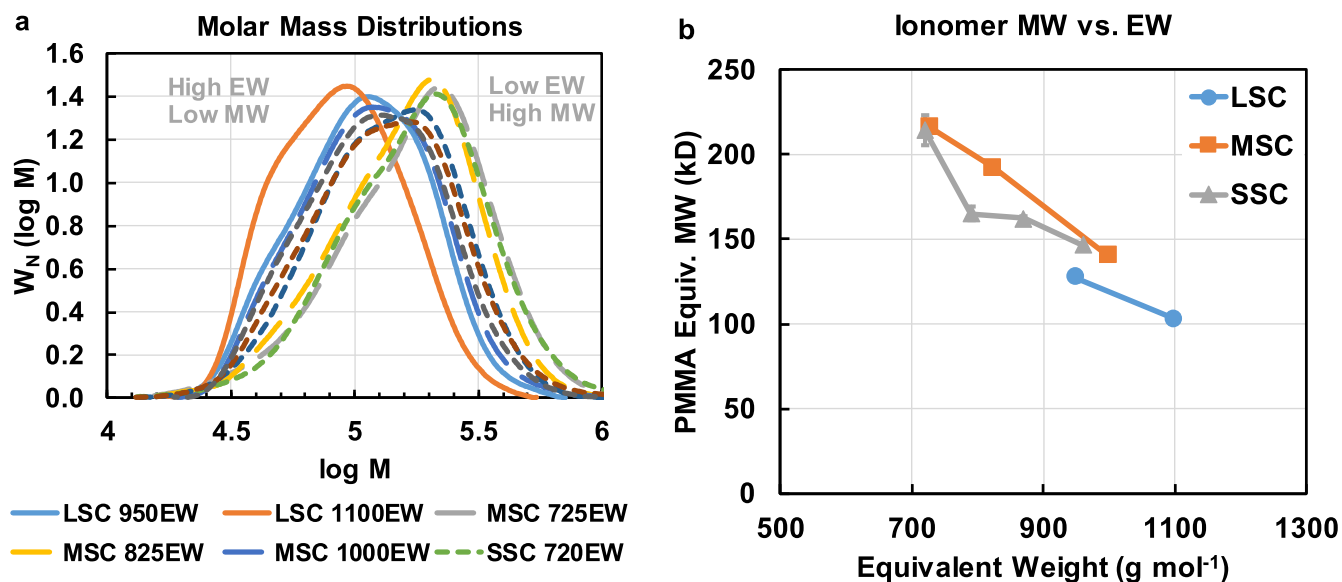


**Figure 2.** Plots showing the results of size exclusion chromatography of dilute ionomer solutions: (a) molecular weight distributions, (b) ionomer molecular weight vs equivalent weight and (c) ionomer intrinsic viscosity vs equivalent weight.

MW<sub>SC</sub>) yield a higher backbone fraction ( $m$ ) and hence, directly affects PFSA crystallinity, glass transition temperature, phase separation etc.<sup>30</sup> Higher crystallinity enables SSC ionomers to be synthesized at lower EW values due to their improved dimensionally stability upon water uptake (i.e. neither dissolve nor become gelatinous). On the other hand, the equation also suggests that for a given side chain length, decreasing EW leads to a lower backbone fraction ( $m$ ).

Figure 2a plots the PMMA-equivalent molecular weight distribution for the ionomer dispersions after dilution to 0.10% PFSA in 80:20 (w/w) n-propanol/water ( $x$ -axis is logarithmic molecular weight ( $M$ ) and  $y$ -axis is weight-averaged molar mass). Figures 2b and 2c show the relationships of the measured PMMA-equivalent molecular weight and ionomer intrinsic viscosity as a function of equivalent weight. As seen in Fig. 2a, the peak in molecular weight gradually shifts from a log  $M$  value of  $\sim 5$  to  $\sim 5.4$  as the ionomer EW decreases from 1000 to 720  $\text{g mmol}^{-1}$ . This transition is seen clearly with the SSC ionomers that is centered around log  $M = 5.1$  for SSC-980EW to log  $M = 5.35$  for SSC-720EW. Intermediate SSC-790EW and SSC-870EW ionomers show a broad shoulder in log  $M$  value from 5 to 5.35. This corresponds to an increase in PMMA-equivalent molecular weight from 100 kD to 215 kD as the ionomer EW decreases from 1100 to 720  $\text{g mmol}^{-1}$  (Fig. 2b). The increase in MW ensures a higher value of parameter  $m$  by virtue of the synthesis process and hence the improved dimensional stability of the ionomer with decreasing EW. Figure 2c shows the intrinsic viscosity of the ionomer which is a direct measure of the ionomer chain expansion and is observed to increase with decreasing EW. Lower EW ionomer has a stronger anion-anion electrostatic repulsion which then further opens the chain conformation in solution thereby leading to increase in viscosity.<sup>47,48</sup>

The scattering profiles for dispersion in Figs. 3a–3c are typical of rod-like particles with ionic groups located at the polymer-solvent interface.<sup>55</sup> The sharp peak observed in the  $0.01 \text{ \AA}^{-1} < q < 0.3 \text{ \AA}^{-1}$  region results from constructive interference between the rod-like particles and is indicative of local ordering of the ionomer rods. For all side-chain lengths, the position of the ionomer peak maximum shifts to lower  $q$  values with increasing EW indicating increasing interparticle spacing between the ionomer rods. While the SSC and LSC ionomer profiles are similar, the MSC profile exhibits a less pronounced interference peak and scattering in the low  $q$  region indicative of less structured spatial arrangement of the rod-like particles and large aggregates, respectively. As noted by Gebel et al.,<sup>56</sup> these two

structural features combine to cause an apparent shift of the ionomer peak to smaller angles (larger distances), an effect that has also been noted when adding salts to ionomer solutions due to screening of the electrostatic repulsions between charged particles.<sup>55</sup> The difference between the SSC and LSC profiles can thus be indicative of lower electrostatic repulsion forces between ionomer rods in the LSC solution. Distinctive features of the MSC profile are the larger slope in the  $0.1$  to  $0.3 \text{ \AA}^{-1}$  region, indicative of a sharper interface between the scatterer and the solvent, and a scattering knee and plateau at  $q < 0.01 \text{ \AA}^{-1}$ , indicative of scattering from a structure with dimensions of  $\sim 100 \text{ nm}$ . This well-defined scattering knee may be attributed to “intrinsic” aggregates of the ionomer rods with well-defined structure and uniform dimensions.<sup>57</sup>

As shown in Fig. 3d, irrespective of side chain length, the rod-like scatterer size and interparticle distance increase with increasing EW to  $\sim 950$ , with invariant values at higher EWs. These results indicate that EW rather than side-chain length is the factor controlling the diameter of the ionomer rods. This is in agreement with conclusions of Loppinet and Gebel from SAXS and SANS studies of PFSA with two different side chain lengths that the rod-like aggregate diameter is proportional to the ionomer EW and, by analogy with other studies of polyethylene-based ionomers, that this is predominantly the effect of EW and not side chain length.<sup>58</sup> This effect of EW has been attributed to changes in the polymer-solvent interfacial energy with changes with charge density on the polymer rod-like aggregate surface (i.e., higher charge density increases solvent interactions and aggregate diameter).<sup>58</sup>

Figures 4a and 4b shows the plot of water uptake (wt.%) and water content ( $\lambda$ ) as a function of ionomer EW. As is seen clearly and expected, decreasing EW leads to higher water uptake and hence, higher  $\lambda$  value.<sup>49,59,60</sup> LSC-950EW ionomer shows the expected  $\lambda$  value of 22  $\text{H}_2\text{O}$  molecules per sulfonic acid ion-exchange site.<sup>61</sup> Ionomers with lower EWs of 720  $\text{g mmol}^{-1}$  indicate a significantly higher  $\lambda$  value of  $\sim 35$  which is in reasonable agreement with literature.<sup>62</sup> Higher MW of the low EW ionomers enable their dimensional stability even at such high  $\lambda$  values. It should be noted that these measurements were carried out by immersing the ionomer membrane in liquid water and not when exposed to water vapor at a defined humidity. Water sorption is a complex, multi-step process that leads to the formation of both the water molecules that are chemically bound to the sulfonic acid site with restricted mobility and the free water in the polymer matrix that exhibit higher mobility and bulk-like behavior.<sup>30</sup> Water sorption by

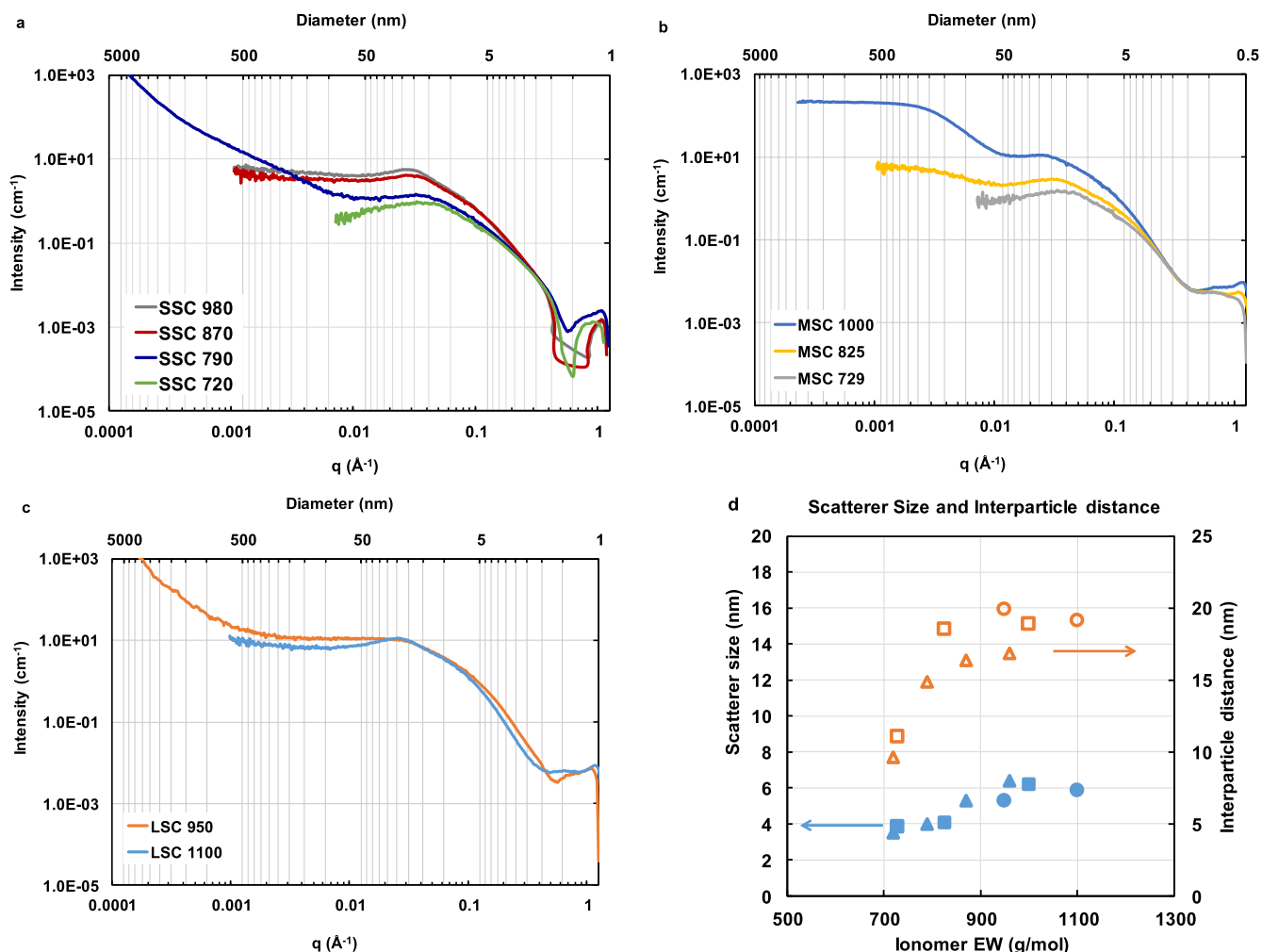


**Figure 3.** (a)–(c) Small angle X-ray scattering spectra of SSC, MSC, LSC length ionomers with various EWs; (d) plot of scatterer size and interparticle distance vs ionomer EW (Circles—LSC, Squares—MSC, Triangles—SSC).

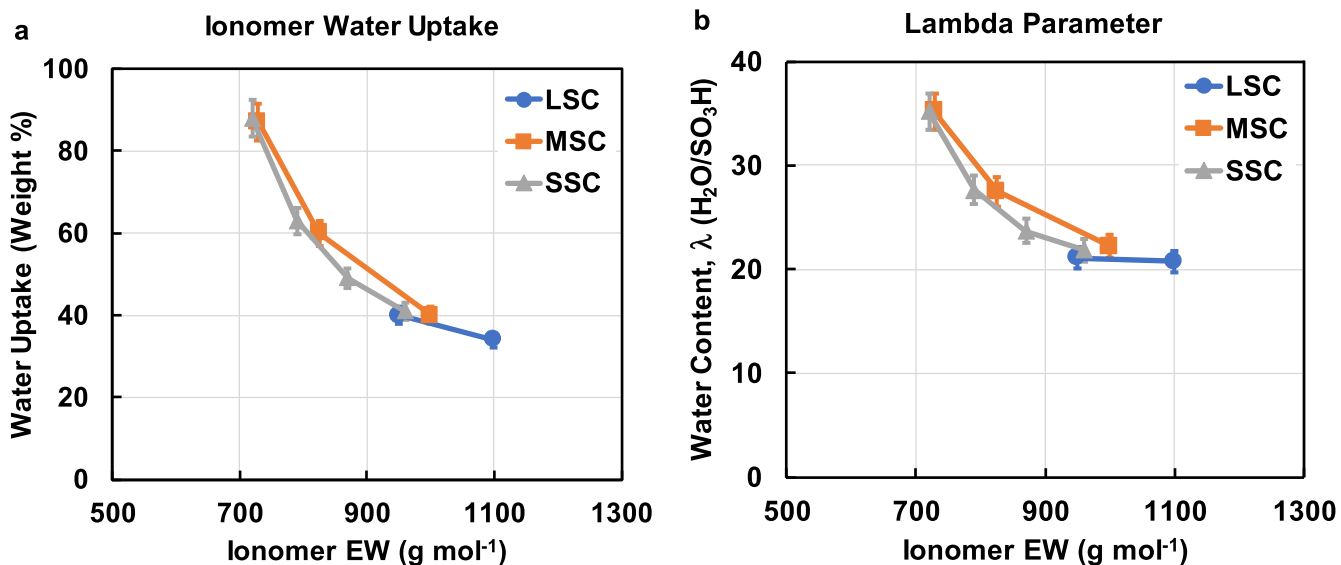


**Figure 4.** Water uptake measurements of the ionomer membranes showing (a) the weight percent of water uptake and (b) the calculated water content or lambda parameter. Water uptake was calculated by measurement the weight gain after immersing the membrane in liquid water at 80 °C for 1 h.

**Table I. Electrochemical diagnostic properties of PtCo/HSC-a cathode catalyst measured in the fuel cell MEA with various ionomers. Anode and cathode loadings of 0.025 and 0.10 mg<sub>Pt</sub> cm<sup>-2</sup>, respectively.**

Ionomer	CO <sub>ads</sub> ECSA (m <sup>2</sup> /g <sub>Pt</sub> ) <sup>a)</sup>	Mass Activity (mA/mg <sub>Pt</sub> ) <sup>b)</sup>	Specific Activity (μA cm <sup>-2</sup> <sub>Pt</sub> ) <sup>b,c)</sup>
LSC-950EW	58.8 ± 3.5	660 ± 40	1719 ± 27
LSC-1100EW	57.5 ± 1.6	546 ± 51	1553 ± 51
MSC-725EW	61.5 ± 0.0	665 ± 10	1580 ± 142
MSC-825EW	63.4 ± 1.6	675 ± 2	1628 ± 135
MSC-1000EW	56.1 ± 0.7	578 ± 16	1723 ± 213
SSC-720EW	62.5 ± 0.2	556 ± 40	1395 ± 34
SSC-790EW	58.3 ± 3.5	513 ± 30	1397 ± 51
SSC-870EW	57.0 ± 0.0	627 ± 23	1563 ± 111
SSC-980EW	57.5 ± 2.4	657 ± 31	1538 ± 171

a) Measured in fuel cell MEA at 30 °C, 100% RH via CO-adsorption/desorption charge integration. b) Measured in fuel cell MEA from H<sub>2</sub>/O<sub>2</sub> polarization curve at 0.9 V<sub>iR-free</sub>, 80 °C, 100% RH, 150 kPa after correction for H<sub>2</sub>-crossover current. c) Specific activity was calculated by dividing mass activity values by the ECSA measured from H<sub>UPD</sub> measurements.

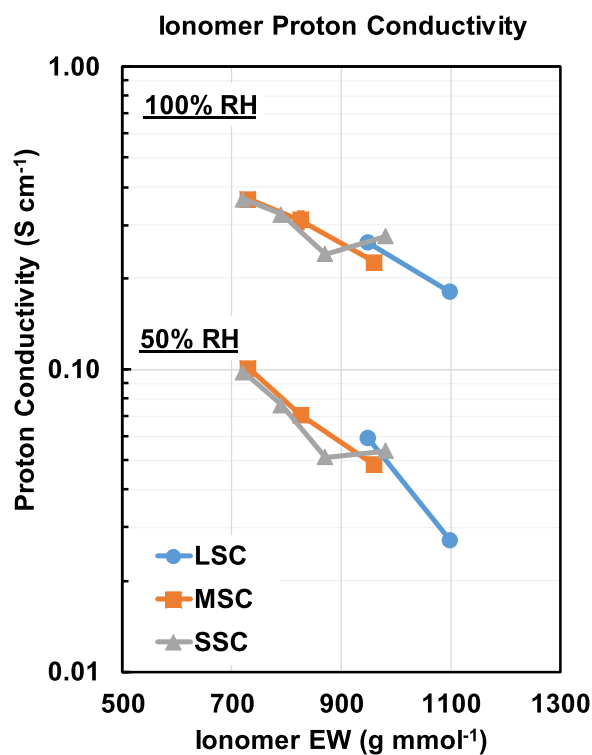


**Figure 5.** H<sup>+</sup> conductivity results of various ionomer membranes measured in a four-probe conductivity setup at 80 °C and two different RH conditions of 50% and 100% RH.

the PFSA is a critical characteristic of the membrane that determines key aspects of its performance such as proton conductivity and reactant transport.

The results of the in-plane proton conductivity of the ionomer measured at 80 °C are shown in Fig. 5 at two different RH conditions of 50% and 100%. At 100% RH, H<sup>+</sup> conductivity increases from 0.18 S cm<sup>-1</sup> for 1100EW ionomer to 0.37 S cm<sup>-1</sup> for 720EW ionomer which represents a factor of two improvement. Improvement factor is even more pronounced (factor ~3.5) at a lower RH of 50%. Ionomer EW plays a significant role in proton conductivity with decreasing EW leading to major improvements in conductivity. These results are as expected since higher water uptake levels sustained by lower EW ionomer enable higher H<sup>+</sup> conductivity. Phase segregation and the formation of hydrophilic water domains consisting of ion-conducting channels is understood to be an important aspect of PFSA ionomer structure that gives rise to its superior proton conductivity. It is suggested here that the low EW

ionomers enhance the formation of interconnected ion-cluster channels due to their higher water uptake and hence, enable higher proton conductivities. The measurements of molecular weight, X-ray scattering profile, water uptake and H<sup>+</sup> conductivity clearly indicate that the ionomer EW is the dominant parameter in determining the physical properties irrespective of the side chain length.

The cathode kinetic properties and H<sub>2</sub>/air polarization performance were measured in a 5 cm<sup>2</sup> MEA active area single cell test fixture. Cathode catalyst material comprised of the 30% PtCo/HSC-a at 0.1 mg<sub>Pt</sub> cm<sup>-2</sup> loading along with one of the various ionomers of interest in this study as described in the Experimental section. Table I summarizes the cathode ECSA measured from CO<sub>ads</sub> stripping measurements along with the kinetic activities measured from H<sub>2</sub>/O<sub>2</sub> polarization curves. ECSA value as measured via CO<sub>ads</sub> stripping measurements at 100% RH indicates a Pt active area in the range of 57 to 63 m<sup>2</sup> g<sup>-1</sup> with no specific trend associated with the use of ionomer. This is as expected since the ECSA is determined largely by the catalyst material which remained the same. The high surface area carbon support used in this study is dominated by internal porosity of <2 nm size with majority of Pt nanoparticle residing in these pores. [10, 11] The effective surface area available for reaction decreases with decreasing RH with Pt particles inside pores becoming inaccessible to proton transport at reduced RH.<sup>11</sup> The mass activity varied in the range of ~550 to 650 mA/mg<sub>Pt</sub> with no specific trend associated with the ionomer EW since the ionomer content in CCL is normalized to the same sulfonic acid content which is in reasonable agreement with the literature.<sup>7</sup> However, we would like to note that this is also contrary to some observations in the literature that suggested the use of low EW ionomer to lead to a drop in kinetic activity due to larger amount of sulfonate functional groups at any given I/C level.<sup>25</sup> While Buchi et al.<sup>41</sup> suggested that lower EW ionomers with lower backbone TFE fraction could be detrimental for low current density operation due to reduced O<sub>2</sub> solubility. Contrarily, Kunal et al.<sup>63</sup> suggested an increase in activity with use of lower EW and SSC ionomer. Also, Kodama et al.<sup>25</sup> suggested that LSC ionomers poison the catalyst surface more strongly due to the higher flexibility of the longer side chain and the presence of two ether linkages. However, our results, within the measurement error, show similar kinetic properties for the ionomers irrespective of their side-chain length and equivalent weight due to the use of optimal ionomer content in the CCL consisting of the same sulfonic acid molality.

Figure 6a shows the H<sub>2</sub>/air polarization curves which does not show any dependence of cell voltage at low current densities (≤0.4 A cm<sup>-2</sup>) in consistency with the kinetic measurements discussed above. Contrarily, the cell voltage at higher current densities (≥1.5 A cm<sup>-2</sup>) show a strong dependence on the type of ionomer, particularly its EW. This is highlighted in Fig. 6b that plots the cell voltage at 2.5 A cm<sup>-2</sup> as a function of ionomer EW. The cell voltage at such high current densities in differential flow cell (5 cm<sup>2</sup> active



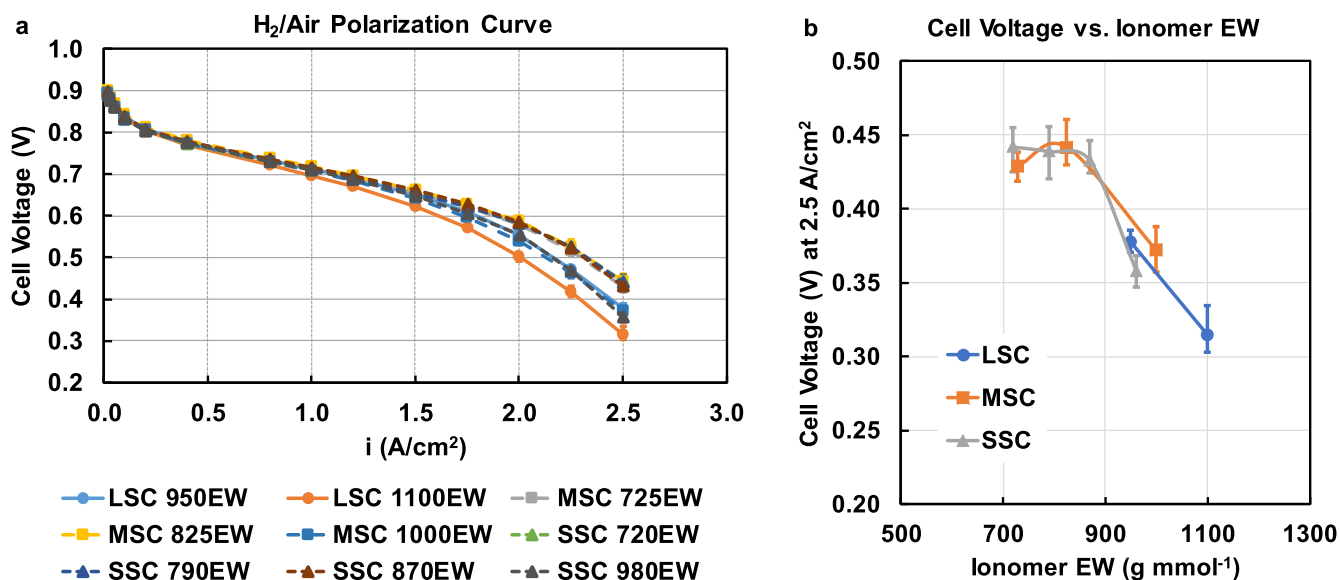


**Figure 6.** (a) H<sub>2</sub>/air polarization curves of MEAs with various ionomers in the cathode catalyst layer and (b) cell voltage from the polarization at 2.5 A cm<sup>-2</sup> vs ionomer EW. Polarization conditions were measured at 80 °C, 100% RH, 150 kPaa, 30% PtCo/HSC-a catalyst at 0.10 mg<sub>Pt</sub> cm<sup>-2</sup> cathode loading.

area with high stoichiometric flows) are dependent on the reactant transport properties such as bulk-H<sup>+</sup> and local-O<sub>2</sub> in the CCL. In general, the cell voltage at 2.5 A cm<sup>-2</sup> increases sharply with decreasing ionomer EW of up to 870 g mmol<sup>-1</sup> below which it remains constant. It is noted that the catalyst layer porosity as measured by mercury intrusion porosimetry measurements indicated a value of 60% for CCLs irrespective of the ionomer used indicating similar bulk transport properties in the secondary pore structure of the catalyst layer. The improvement in cell voltage at high current densities with decreasing EW is likely a combination of both improved proton transport and local-O<sub>2</sub> transport properties imparted by the ionomer as discussed below.

Figure 7a shows a semi-log plot of the through-plane proton transport resistance ( $R_{H^+,cathode}$ ) in the ionomer phase of the catalyst layer as a function of RH measured via the H<sub>2</sub>/N<sub>2</sub> impedance methodology. Figure 7b plots the H<sup>+</sup> transport resistance as a function of ionomer EW at two different RH conditions. As expected, the H<sup>+</sup> transport resistance decreases with increasing

RH and decreasing ionomer EW in qualitative consistency with the ex situ ionomer conductivity determined using the four-probe conductivity measurements. This is also in qualitative agreement with the water uptake measurements that showed an increasing  $\lambda$  value with decreasing EW that would enable lower H<sup>+</sup> transport resistances in CCL.

Figure 8a shows a representative plot of the pressure-independent O<sub>2</sub> transport resistance for the various ionomers as a function of inverse roughness factor. As explained in the experimental section above, the slope of this plot provides a direct measure of  $R_{O_2-local}$  which is a pressure-independent parameter that can be used to quantify the resistance towards O<sub>2</sub> transport at or near the Pt catalyst surface.<sup>3</sup> This interfacial resistance could arise due to O<sub>2</sub> transport through the ionomer thin film covering the catalyst particles ( $R_{Pt-ionomer}$ ) and/or within the micro/mesoporous carbon structure ( $R_{Pt-interior}$ ) to reach the Pt active site. The resistance term  $R_{Pt-ionomer}$  corresponds only to the fraction of Pt present on the external surface of the carbon support that is in direct contact with the ionomer and is

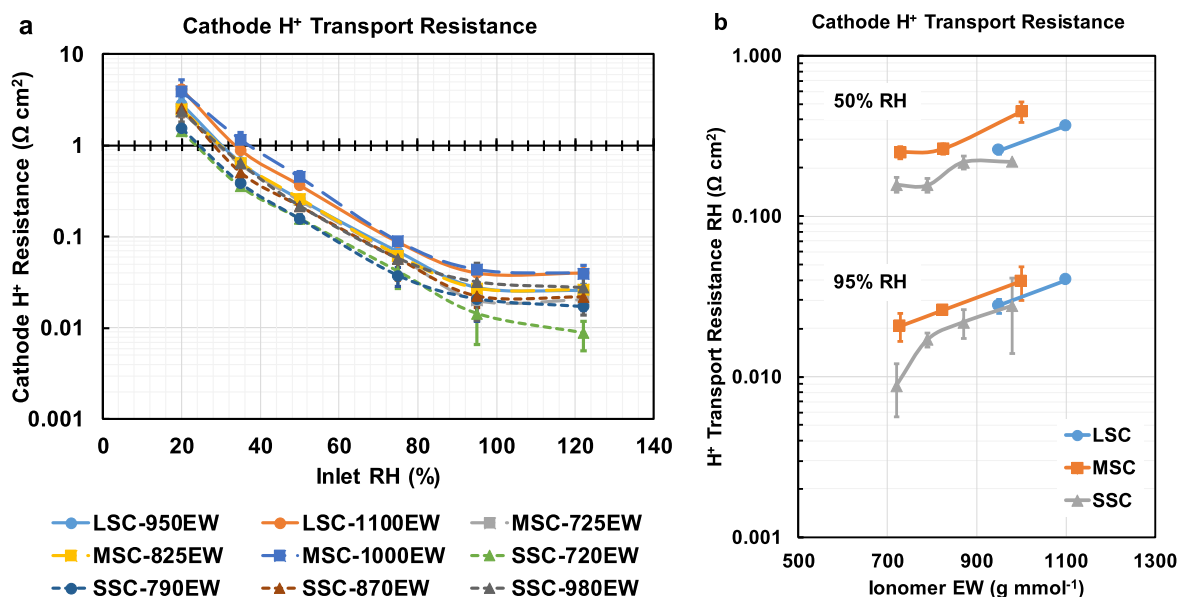


**Figure 7.** (a) Semi-log plot of the bulk-H<sup>+</sup> transport resistance of the cathode catalyst layer vs inlet relative humidity and (b) bulk-H<sup>+</sup> transport resistance vs ionomer EW at two different RH values of 50% and 95% RH.

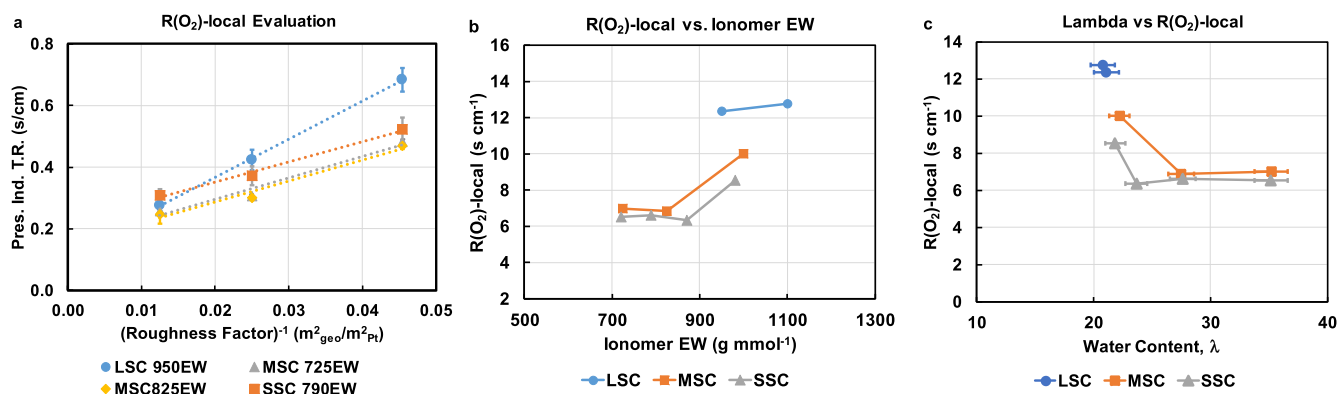


**Figure 8.** Measurement of local-O<sub>2</sub> transport resistance. (a) Representative plot of pressure independent O<sub>2</sub> transport resistance vs inverse roughness factor. Correlation of local-O<sub>2</sub> transport resistances vs (b) ionomer EW and (c) membrane water content (lambda parameter).

not applicable to the Pt nanoparticles present in the internal of the carbon primary particles. Conversely,  $R_{\text{Pt-interior}}$  corresponds only to the fraction of Pt nanoparticles that is present in the interior volume of the carbon primary particle that does not directly contact the ionomer film. Since the same PtCo/HSC-a catalyst was used,  $R_{\text{Pt-interior}}$  is expected to be constant for electrodes with changing ionomers. As can be seen in Fig. 8a, the slope of the plot is dependent on the ionomer EW. For instance, the LSC-950EW ionomer yields a slope of  $12.7 \text{ S cm}^{-1}$  whereas the lower EW ionomers (MSC 725EW, SSC 790EW) show a lower slope of  $\sim 7 \text{ S cm}^{-1}$ . An attempt was made to correlate the  $R_{\text{O}_2\text{-local}}$  to EW and the  $\lambda$  parameter of the ionomer as shown in Figs. 8b and 8c. Interestingly, the measured  $R_{\text{O}_2\text{-local}}$  decreases with decreasing EW up to  $870 \text{ g mmol}^{-1}$  and remains constant below that. In other words,  $R_{\text{O}_2\text{-local}}$  decreases with increasing  $\lambda$  value up to  $\sim 24$  and remains constant above that. This correlation suggests that as the ionomer EW decreases, it retains more H<sub>2</sub>O molecules per SO<sub>3</sub>H site that translates to a lower local-O<sub>2</sub> transport resistance in the catalyst layer. However, for  $\lambda$  values between 20–24, ionomers show distinctly different  $R_{\text{O}_2\text{-local}}$ , from which emerges the effect of side-chain: for a comparable level of hydration in ionomers,  $R_{\text{O}_2\text{-local}}$  increases with increasing side-chain length. To examine the structural origins of this transport resistance, nanomorphology of ionomers cast as 60–100 nm thin-film on Si(O<sub>2</sub>) is investigated using GISAXS. From the 2D GISAXS spectra collected at 95% RH, several structural parameters were extracted and plotted in Fig. 9. Domain spacing of ionomer thin-films exhibit a relatively weaker dependence on EW, but for a given EW, d-spacing decreases with reduced side-chain length, with the SSC ionomer possessing the lowest value. The smaller domain spacing and larger FWHM indicates less well-ordered phase-separation through-plane. Less distinct layering of hydrophilic and hydrophobic domains through-plane would lead to reduced transport resistance in catalyst-ionomer in agreement with the trends observed for  $R_{\text{O}_2\text{-local}}$ .

It was demonstrated recently that some of the structural changes observed herein occur during ionomer film formation which is governed by mechanism rooted in the dispersion behavior.<sup>64</sup> Thus, this paper's findings demonstrating that ionomer chemistry affects both dispersion properties and catalyst ionomer structure and properties is critical for evidencing a linkage between dispersion characteristic and cell performance.

It has been hypothesized in the literature that due to the spatial confinement and surface adsorption effects, PFSA ionomer thin film in the catalyst layer loses its ability to phase segregate leading to a stiffer backbone, decreased water uptake and increases in O<sub>2</sub>/H<sub>2</sub>O transport resistances.<sup>1,30</sup> Based on our experimental results, it can be suggested that the use of low EW ionomer in the catalyst layer leads to higher water uptake and maintains a more hydrated state that enables improved O<sub>2</sub> transport properties. The improved O<sub>2</sub> transport properties are also likely from the higher O<sub>2</sub> diffusion rates and

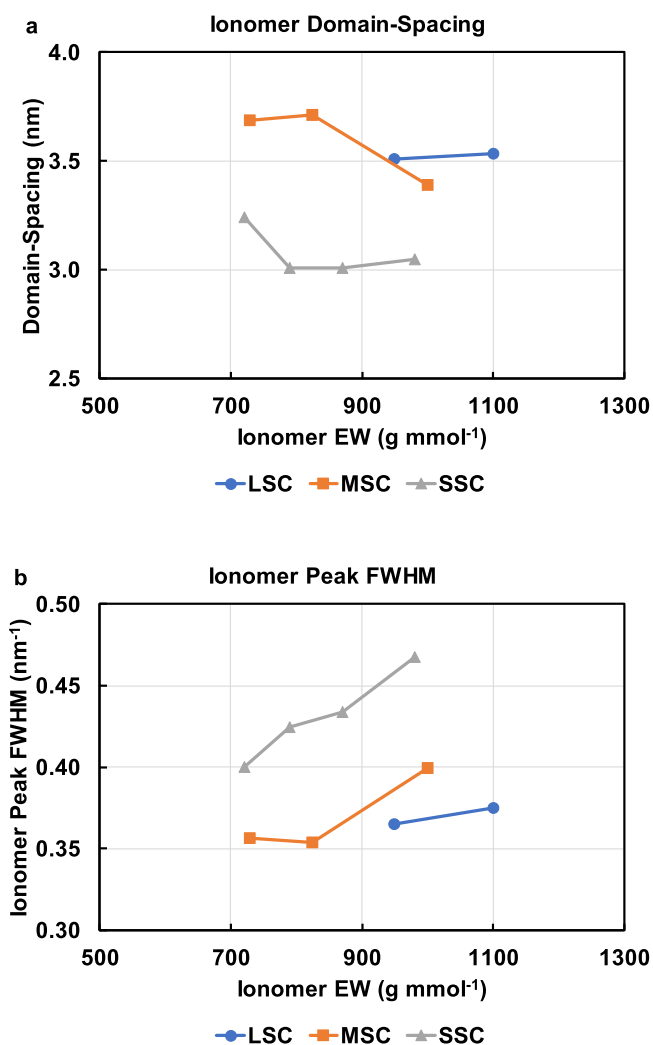


**Figure 9.** Structural parameters of ionomer thin-films cast on Si(O<sub>2</sub>) determined from GISAXS data collected at 95% RH. Through-plane (a) domain spacing and (b) full-width half max of ionomer thin films.

O<sub>2</sub> permeability rates observed for lower EW ionomers with higher fraction of water content ( $\lambda$ ).<sup>41</sup>

Based on the experimental results above, ionomer EW is a dominant factor in determining its molecular weight, intrinsic viscosity, scatterer size and interparticle distance, water uptake, proton conductivity, local-O<sub>2</sub> transport resistance, and eventually the

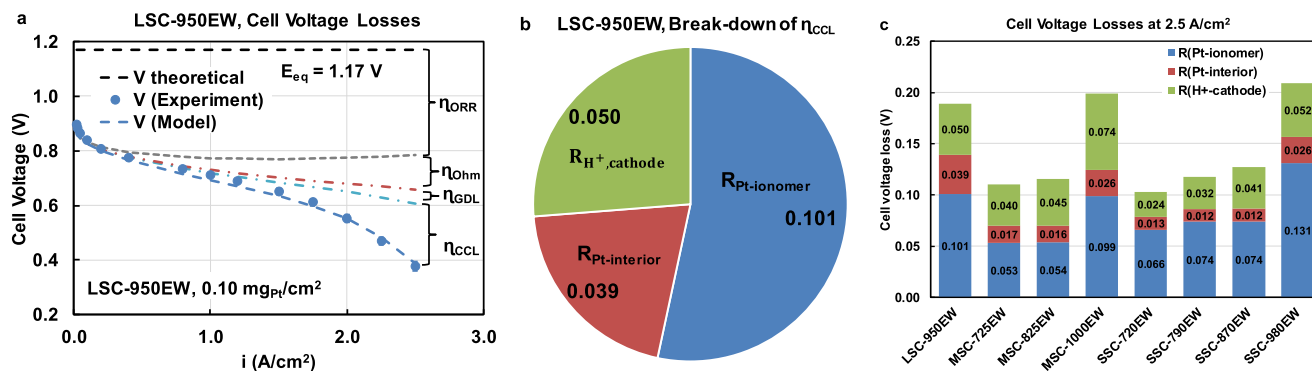


**Figure 10.** Cell voltage losses due to the various reactant transport resistances in the CCL at  $2.5 \text{ A cm}^{-2}$  predicted by the 1D-performance model. (a)  $\text{H}_2/\text{air}$  polarization curve for 30% PtCo/HSC-a catalyst with LSC-950EW ionomer showing the comparison between experimentally measured and 1D-performance model-predicted cell voltage along with the cell voltage loss factors. (Cell voltage losses due to  $\eta_{\text{ORR}}$ —ORR kinetics,  $\eta_{\text{Ohm}}$ —Ohmic resistance,  $\eta_{\text{GDL}}$ — $\text{O}_2$  bulk transport loss in GDL,  $\eta_{\text{CCL}}$ —sum of cathode catalyst layer losses that includes  $R_{\text{H}^+, \text{cathode}}$ ,  $R_{\text{Pt-ionomer}}$ ,  $R_{\text{Pt-interior}}$ .) (b) Break-down of HCD cell voltage losses in CCL corresponding to  $\eta_{\text{CCL}}$ . (c) Break-down of HCD cell voltage losses corresponding to  $\eta_{\text{CCL}}$  for all the ionomer at  $2.5 \text{ A cm}^{-2}$ . Operating conditions, 30% PtCo/HSC-a catalyst,  $0.10 \text{ mg}_{\text{Pt}} \text{ cm}^{-2}$ ,  $\text{H}_2/\text{air}$ ,  $80^\circ \text{C}$ , 100%  $\text{RH}_{\text{inlet}}$ ,  $150 \text{ kPa}_{\text{outlet}}$ , high stoichiometric differential cell flow conditions.

cell voltage in MEA. Specifically, ionomer MW, intrinsic viscosity, water uptake and  $\text{H}^+$  conductivity tend to increase monotonically with decreasing EW. Cell voltage at  $2.5 \text{ A cm}^{-2}$  increase sharply with decreasing EW up to  $\sim 870$  and remains constant below that. Conversely,  $R_{\text{O}_2\text{-local}}$  decreases sharply with decreasing EW up to  $\sim 870$  and remains constant below that. It can be summarized that increasing water uptake with decreasing EW leads to a decrease in bulk- $\text{H}^+$  and local- $\text{O}_2$  transport resistances that enable improvements in cells voltages at higher current densities.

An earlier study by Ohma et al. on the impact of ionomer EW concluded that the local- $\text{O}_2$  transport resistance increased with decreasing ionomer EW. A constant of I/C level of 0.9 was used for ionomers of varying EWs from  $\sim 550$  to  $1100 \text{ g mmol}^{-1}$ .<sup>65</sup> We believe that the use of same I/C levels for ionomers with such large variation in EW gave rise to a non-optimal secondary pore structures with significantly high gas transport resistances leading to conclusions contrary to ours. The use of constant sulfonic acid molality in the CCL rather than a constant I/C level in our study avoids such errors and leads to a clear conclusion that decrease in ionomer EW enables lower local- $\text{O}_2$  transport resistances.

A 1D-performance model was used to fit the experimental polarization curves and understand the various cell voltage loss factors (see Appendix for details). Figure 10a shows a good agreement between the experimental and model performance of LSC-950EW ionomer along with a breakdown of the various resistance that contribute to the cell voltage losses. As described in the Appendix, the model considers ORR current distribution between interior and exterior Pt particles. It is assumed that a  $R_{\text{O}_2\text{-local}}$  exists due to  $\text{O}_2$  transport losses at the Pt-ionomer interface ( $R_{\text{Pt-ionomer}}$ ) and/or within the micro/mesoporous carbon structure ( $R_{\text{Pt-interior}}$ ). Therefore,  $R_{\text{Pt-ionomer}}$  is a local resistance that does not apply to the interior Pt in the absence of ionomer coverage. Instead, it is the effective oxygen permeability in micro/mesopores that determines the effectiveness of the interior Pt ( $R_{\text{Pt-interior}}$ ), which results in a respective voltage loss. While the voltage loss due to the sluggish ORR kinetics remains the largest factor contributing  $\sim 400 \text{ mV}$  at  $2.5 \text{ A cm}^{-2}$ , the 1D-performance model identifies several transport-related factors specifically in the CCL (Fig. 10b). For instance in the case of LSC-950EW ionomer, cell voltage loss due to  $R_{\text{O}_2\text{-local}}$  amounts to  $140 \text{ mV}$  at  $2.5 \text{ A cm}^{-2}$  which includes contributions from both the  $R_{\text{Pt-ionomer}}$  ( $101 \text{ mV}$ ) and  $R_{\text{Pt-interior}}$  ( $39 \text{ mV}$ ); further,  $R_{\text{H}^+, \text{cathode}}$  due to  $\text{H}^+$ -transport loss in the cathode amounts to  $50 \text{ mV}$ . Figure 10c shows the mass transport related cell voltage losses in the CCL at  $2.5 \text{ A cm}^{-2}$  for all the ionomers. For any given side chain length, the cell voltage loss due to the bulk- $\text{H}^+$  and local- $\text{O}_2$  transport resistances decrease with decreasing EW. Specifically, the decrease in cell voltage loss is significant as the EW

decreases from  $\sim 1000$  to below  $900 \text{ EW}$ . For instance, cell voltage loss arising from local- $\text{O}_2$  transport resistance for SSC ionomers decreases sharply from  $131 \text{ mV}$  at  $980 \text{ EW}$  to  $74 \text{ mV}$  for  $870 \text{ EW}$  below which it is relatively constant. This is in good agreement with the experimentally measured cell voltages and  $R_{(\text{O}_2\text{-local})}$  results discussed above. This clearly shows that the HCD mass transport issues in the CCL are strongly dependent on the ionomer EW.

## Conclusions

The impact of PFSA ionomers with varying side-chain lengths and EWs on the CCL properties have been studied in detail, particularly for the local- $\text{O}_2$  transport resistance and the high-current density performance. These results clearly indicate that the PFSA ionomer EW is a dominant property determining a suite of physico-chemical properties that directly impact the bulk- $\text{H}^+$  and local- $\text{O}_2$  transport resistance in the CCL and hence, the polarization performance at high current densities. Specifically, decreasing ionomer EW leads to an increase in its molecular weight, intrinsic viscosity and water uptake. This enables lower bulk- $\text{H}^+$  and local- $\text{O}_2$  transport resistances in the CCL with decreasing EW. No impact of ionomer EW was observed on the cathode kinetic properties. Consequently, lower voltage losses due to bulk- $\text{H}^+$  and local- $\text{O}_2$  transport resistance are observed at high current densities for catalyst layers with lower EW ionomer.

## Acknowledgments

This work was partially supported by U.S. Department of Energy, Office of Energy Efficiency and Renewable Energy under grant DE-EE0007651. The Argonne work was supported by the U.S. DOE Energy Efficiency and Renewable Energy, Hydrogen and Fuel Cell Technologies Office through the Fuel Cell Performance and Durability (FC-PAD) consortium. USAXS measurements used the resources of the Advanced Photon Source, a U.S. DOE Office of Science User Facility operated for the DOE Office of Science by Argonne National Laboratory under Contract No. DE-AC02-06CH11357. NR would like to acknowledge Drs. Craig Gittleman, Ruichun Jiang for useful discussions and Ratandeep Singh Kukreja, Cristin Keary, Kathryn Stevick, Peter Harvey, David Lindsey, Kenneth Holt of GM for analytical and engineering support. DM and NK would like to thank Jan Ilavsky and Ivan Kuzmenko of the APS beam line 9-ID-C.

## Appendix

**Model development.**—In our previous paper,<sup>11</sup> we described an electrode model that considers catalyst morphology, particularly

accounting for ORR taking place at both interior and exterior Pt surfaces. Whereas ORR current at the exterior Pt surface is affected by the local oxygen transport resistance ( $R_{\text{Pt-ionomer}}$ ) due to Pt-ionomer interaction, an overall effectiveness factor is evaluated based on  $\text{O}_2$  transport through micro-/meso-pores of HSC particles for the interior Pt. The effective oxygen permeability in micro-/meso-pores (relating to porosity/tortuosity) was obtained by fitting to the measured polarization curves. In this work, instead of tuning porosity/tortuosity, we have developed a semi-empirical correlation for the overall effectiveness factor of interior Pt in terms of Pt loading ( $L_{\text{Pt}}$ ), electrochemically active area (ECA), and applied current density ( $i_{\text{app}}$ )

$$\Theta = f(L_{\text{Pt}}, \text{ECA}, i_{\text{app}}) \quad [\text{A-1}]$$

utilizing the experimental data (polarization curves, ECSA, specific activity, electrode  $\text{H}^+$  resistance, and  $R_{\text{O}_2\text{-local}}$ ) taken from cells built with Pt/HSC catalyst at both BOL and EOT.

**Impact of Co cation contamination.**—With the above-obtained overall effectiveness factor for interior Pt, one can further utilize the experimental data taken from cells built with PtCo/HSC catalyst to develop a semi-empirical correlation for the effect of  $\text{Co}^{2+}$  contamination. As electrode degrades, Co cations leach out of PtCo/HSC catalyst and contaminate ionomer by occupying proton sites. This would result in lowered activity of protons involved in ORR and thus incur a higher kinetic loss. In an extreme scenario, cations are driven towards cathode and effectively deactivate a portion of cathode adjacent to MPL,<sup>66</sup> which would cause a large voltage loss at a high current density. Furthermore, lower relative humidity (RH) in cathode catalyst layer leads to more ORR closer to membrane, which would incur additional voltage loss. Therefore, we evaluate the effective Pt loading under the influence of the mole fraction of proton sites occupied by Co cation ( $x_{\text{Co}}$ ), applied current density ( $i_{\text{app}}$ ), and cathode RH ( $\text{RH}_{\text{cath}}$ )

$$L_{\text{Pt}}^{\text{eff}}/L_{\text{Pt}} = f(x_{\text{Co}}, i_{\text{app}}, \text{RH}_{\text{cath}}) \quad [\text{A-2}]$$

which is then used in Eq. A-1 for calculating the overall effectiveness factor for interior Pt.

**Effect of ionomer EW.**—Given I/C and ionomer EW, the volume fraction of ionomer in an electrode can be calculated by,<sup>53</sup>

$$\varepsilon_i = (I/C) \cdot \frac{10}{f_t d_{m,\text{dry}}} \cdot \left( 1 + \frac{M_w \cdot d_{m,\text{dry}} \cdot \lambda}{d_w \cdot \text{EW}} \right) \quad [\text{A-3}]$$

where I/C is the weight ratio of ionomer to carbon in the electrode,  $f_t$  is  $28 \pm 2 \mu\text{m}/(\text{mg}_C \text{ cm}^{-2})$  for  $I/C < 3/1$ ,  $d_{m,\text{dry}}$  is the density of dry ionomer,  $d_w$  is the density of water,  $M_w$  is the molecular weight of water, and  $\lambda$  is water content depending strongly on RH. According to Eq. A-3, volume fraction of ionomer is proportional to I/C ratio and inversely proportional to EW (due to larger swelling at lower EWs). At a given  $\lambda$ , lower EW and higher I/C lead to a higher volume fraction of ionomer which effectively decreases electrode porosity, thus increasing local oxygen transport resistance and tendency to agglomerate (or equivalently reduced amount of interior Pt). Therefore, one can use the following empirical correlations to account for the effect of ionomer EW

$$R_{\text{O}_2\text{-local}}^{\text{eff}}/R_{\text{O}_2\text{-local}} = f(\varepsilon_i, i_{\text{app}}) \quad [\text{A-4}]$$

and

$$L_{\text{Pt, int}}^{\text{eff}}/L_{\text{Pt, int}} = f(\varepsilon_i, i_{\text{app}}) \quad [\text{A-5}]$$

Here,  $i_{\text{app}}$  is included as the impact of  $\text{O}_2$  transport resistance which increases with current density.

## ORCID

Nagappan Ramaswamy  <https://orcid.org/0000-0002-3430-2758>  
 Nancy Kariuki  <https://orcid.org/0000-0002-6123-7373>  
 Deborah Myers  <https://orcid.org/0000-0001-9299-3916>  
 Ahmet Kusoglu  <https://orcid.org/0000-0002-2761-1050>

## References

1. A. Kongkanand and M. F. Mathias, "The priority and challenge of high-power performance of low-platinum proton-exchange membrane fuel cells." *J. Phys. Chem. Lett.*, **7**, 1127 (2016).
2. O. Gröger, H. A. Gasteiger, and J.-P. Suchsland, "Review—electromobility: batteries or fuel cells?" *J. Electrochem. Soc.*, **162**, A2605 (2015).
3. T. A. Greszler, D. Caulk, and P. Sinha, "The impact of platinum loading on oxygen transport resistance." *J. Electrochem. Soc.*, **159**, F831 (2012).
4. A. Ohma, T. Mashio, K. Sato, H. Iden, Y. Ono, K. Sakai, K. Akizuki, S. Takaichi, and K. Shinohara, "Analysis of proton exchange membrane fuel cell catalyst layers for reduction of platinum loading at Nissan." *Electrochim. Acta*, **56**, 10832 (2011).
5. A. Z. Weber and A. Kusoglu, "Unexplained transport resistances for low-loaded fuel-cell catalyst layers." *J. Mater. Chem. A*, **2**, 17207 (2014).
6. H. Iden, T. Mashio, and A. Ohma, "Gas transport inside and outside carbon supports of catalyst layers for PEM fuel cells." *J. Electroanal. Chem.*, **708**, 87 (2013).
7. S. Jomori, K. Komatsubara, N. Nonoyama, M. Kato, and T. Yoshida, "An experimental study of the effects of operational history on activity changes in a PEMFC." *J. Electrochem. Soc.*, **160**, F1067 (2013).
8. T. Soboleva, X. Zhao, K. Malek, Z. Xie, T. Navessin, and S. Holdcroft, "On the micro-, meso-, and macroporous spatial distributions of Pt catalyst nanoparticles on carbon substrates in polymer electrolyte fuel cells." *ACS Appl. Mater. Interfaces*, **2**, 375 (2010).
9. T. Ito, U. Matsuwaki, Y. Otsuka, M. Hatta, K. Hayakawa, K. Matsutani, T. Tada, and H. Jinnai, "Three-dimensional spatial distributions of Pt catalyst nanoparticles on carbon substrates in polymer electrolyte fuel cells." *Electrochemistry*, **79**, 374 (2011).
10. E. Padgett et al., "Editors' choice—connecting fuel cell catalyst nanostructure and accessibility using quantitative Cryo-STEM tomography." *J. Electrochem. Soc.*, **165**, F173 (2018).
11. N. Ramaswamy, W. Gu, J. M. Ziegelbauer, and S. Kumaraguru, "Carbon support microstructure impact on high current density transport resistances in PEMFC cathode." *J. Electrochem. Soc.*, **167**, 064515 (2020).
12. V. Yarlagadda, M. K. Carpenter, T. E. Moylan, R. S. Kukreja, R. Koestner, W. Gu, L. Thompson, and A. Kongkanand, "Boosting fuel cell performance with accessible carbon mesopores." *ACS Energy Lett.*, **3**, 618 (2018).
13. H. Iden, K. Sato, A. Ohma, and K. Shinohara, "Relationship among microstructure, ionomer property and proton transport in Pseudo catalyst layers." *J. Electrochem. Soc.*, **158**, B987 (2011).
14. H. Iden and A. Ohma, "An in situ technique for analyzing ionomer coverage in catalyst layers." *J. Electroanal. Chem.*, **693**, 34 (2013).
15. M. Lopez-Haro, L. Guétaz, T. Printemps, A. Morin, S. Escribano, P. H. Jouneau, P. Bayle-Guillemaud, F. Chandezon, and G. Gebel, "Three-dimensional analysis of nafion layers in fuel cell electrodes." *Nat. Commun.*, **5**, 5229 (2014).
16. K. Shinozaki, Y. Morimoto, B. S. Pivovarov, and S. S. Kocha, "Suppression of oxygen reduction reaction activity on Pt-based electrocatalysts from ionomer incorporation." *J. Power Sources*, **325**, 745 (2016).
17. T. Masuda, H. Naohara, S. Takakusagi, P. R. Singh, and K. Uosaki, "Formation and structure of perfluorosulfonated ionomer thin film on a graphite surface." *Chem. Lett.*, **38**, 884 (2009).
18. A. Ohma, K. Fushinobu, and K. Okazaki, "Influence of Nafion® film on oxygen reduction reaction and hydrogen peroxide formation on Pt electrode for proton exchange membrane fuel cell." *Electrochim. Acta*, **55**, 8829 (2010).
19. T. Masuda, F. Sonsudin, P. R. Singh, H. Naohara, and K. Uosaki, "Potential-dependent adsorption and desorption of perfluorosulfonated ionomer on a platinum electrode surface probed by electrochemical quartz crystal microbalance and atomic force microscopy." *J. Phys. Chem. C*, **117**, 15704 (2013).
20. Y. Ayato, K. Kunimatsu, M. Osawa, and T. Okada, "Study of Pt electrode/nafion ionomer interface in HClO[Sub 4] by in situ surface-enhanced FTIR spectroscopy." *J. Electrochem. Soc.*, **153**, A203 (2006).
21. D. Malevich, V. Zamylny, S. G. Sun, and J. Lipkowski, "In Situ Infrared Reflection Absorption Spectroscopy Studies of the Interaction of Nafion® with the Pt Electrode Surface." *Zeitschrift für Phys. Chemie*, **217**, 513 (2003).
22. R. Subbaraman, D. Strmcnik, A. P. Paulikas, V. R. Stamenkovic, and N. M. Markovic, "Oxygen reduction reaction at three-phase interfaces." *ChemPhysChem*, **11**, 2825 (2010).
23. R. Subbaraman, D. Strmcnik, V. Stamenkovic, and N. M. Markovic, "Three phase interfaces at electrified metal-solid electrolyte systems I. Study of the Pt(Hkl)-Nafion interface." *J. Phys. Chem. C*, **114**, 8414 (2010).
24. T. R. Garrick, T. E. Moylan, V. Yarlagadda, and A. Kongkanand, "Characterizing electrolyte and platinum interface in PEM fuel cells Using CO displacement." *J. Electrochem. Soc.*, **164**, F60 (2017).
25. K. Kodama, K. Motobayashi, A. Shinohara, N. Hasegawa, K. Kudo, R. Jinnouchi, M. Osawa, and Y. Morimoto, "Effect of the side-chain structure of perfluoro-sulfonic acid ionomers on the oxygen reduction reaction on the surface of Pt." *ACS Catal.*, **8**, 694 (2018).
26. I. Kendrick, D. Kumari, A. Yakoboski, N. Dimakis, and E. S. Smotkin, "Elucidating the ionomer-electrified metal interface." *J. Am. Chem. Soc.*, **132**, 17611 (2010).
27. H. Hanawa, K. Kunimatsu, M. Watanabe, and H. Uchida, "In situ ATR-FTIR analysis of the structure of Nafion-Pt/C and Nafion-Pt 3Co/C interfaces in fuel cell." *J. Phys. Chem. C*, **116**, 21401 (2012).

28. H. Iden, S. Takaichi, Y. Furuya, T. Mashio, Y. Ono, and A. Ohma, "Relationship between gas transport resistance in the catalyst layer and effective surface area of the catalyst." *J. Electroanal. Chem.*, **694**, 37 (2013).
29. A. Kongkanand, V. Yarlagadda, T. R. Garrick, T. E. Moylan, and W. Gu, "(Plenary) Electrochemical diagnostics and modeling in developing the PEMFC cathode." *ECS Trans.*, **75**, 25 (2016).
30. A. Kusoglu and A. Z. Weber, "New insights into perfluorinated sulfonic-acid ionomers." *Chem. Rev.*, **117**, 987 (2017).
31. K. A. Page, A. Kusoglu, C. M. Stafford, S. Kim, R. J. Kline, and A. Z. Weber, "Confinement-driven increase in ionomer thin-film modulus." *Nano Lett.*, **14**, 2299 (2014).
32. A. Kusoglu, D. Kushner, D. K. Paul, K. Karan, M. A. Hickner, and A. Z. Weber, "Impact of substrate and processing on confinement of nafion thin films." *Adv. Funct. Mater.*, **24**, 4763 (2014).
33. M. Bass, A. Berman, A. Singh, O. Konovalov, and V. Freger, "Surface-induced micelle orientation in nafion films." *Macromolecules*, **44**, 2893 (2011).
34. K. Kodama, R. Jinnouchi, T. Suzuki, H. Murata, T. Hatanaka, and Y. Morimoto, "Increase in adsorptivity of sulfonate anions on Pt (111) surface with drying of ionomer." *Electrochem. Commun.*, **36**, 26 (2013).
35. J. Zhang, B. A. Litteer, F. D. Coms, and R. Makharia, "Recoverable performance loss due to membrane chemical degradation in PEM fuel cells." *J. Electrochem. Soc.*, **159**, F287 (2012).
36. K. Kodama, A. Shinohara, N. Hasegawa, K. Shinozaki, R. Jinnouchi, T. Suzuki, T. Hatanaka, and Y. Morimoto, "Catalyst Poisoning Property of Sulfonimide Acid Ionomer on Pt (111) Surface." *J. Electrochem. Soc.*, **161**, F649 (2014).
37. Y. Garsany, R. W. Atkinson, M. B. Sassin, R. M. E. Hjelm, B. D. Gould, and K. E. Swider-Lyons, "Improving PEMFC performance using short-side-chain low-equivalent-weight PFSA ionomer in the cathode catalyst layer." *J. Electrochem. Soc.*, **165**, F381 (2018).
38. C. Lei, D. Bessarabov, S. Ye, Z. Xie, S. Holdcroft, and T. Navessin, "Low equivalent weight short-side-chain perfluorosulfonic acid ionomers in fuel cell cathode catalyst layers." *J. Power Sources*, **196**, 6168 (2011).
39. A. Orfanidi, P. Madkikar, H. A. El-Sayed, G. S. Harzer, T. Kratky, and H. A. Gasteiger, "The key to high performance low Pt loaded electrodes." *J. Electrochem. Soc.*, **164**, F418 (2017).
40. T. Van Cleve et al., "Dictating Pt-Based electrocatalyst performance in polymer electrolyte fuel cells, from formulation to application." *ACS Appl. Mater. Interfaces*, **11**, 46953 (2019).
41. F. N. Büchi, M. Wakizoe, and S. Srinivasan, "Microelectrode investigation of oxygen permeation in perfluorinated proton exchange membranes with different equivalent weights." *J. Electrochem. Soc.*, **143**, 927 (1996).
42. H. Xu, H. R. Kunz, L. J. Bonville, and J. M. Fenton, "Improving PEMFC performance using low equivalent weight PFSA ionomers and Pt-CoC catalyst in the cathode." *J. Electrochem. Soc.*, **154**, B271 (2007).
43. J. Peron, D. Edwards, M. Haldane, X. Luo, Y. Zhang, S. Holdcroft, and Z. Shi, "Fuel cell catalyst layers containing short-side-chain perfluorosulfonic acid ionomers." *J. Power Sources*, **196**, 179 (2011).
44. A. Stassi, I. Gatto, E. Passalacqua, V. Antonucci, A. S. Arico, L. Merlo, C. Oldani, and E. Pagano, "Performance comparison of long and short-side chain perfluorosulfonic membranes for high temperature polymer electrolyte membrane fuel cell operation." *J. Power Sources*, **196**, 8925 (2011).
45. Y. C. Park, K. Kakinuma, H. Uchida, M. Watanabe, and M. Uchida, "Effects of short-side-chain perfluorosulfonic acid ionomers as binders on the performance of low Pt loading fuel cell cathodes." *J. Power Sources*, **275**, 384 (2015).
46. Y. Jeon, H. K. Hwang, J. Park, H. Hwang, and Y. G. Shul, "Temperature-dependent performance of the polymer electrolyte membrane fuel cell using short-side-chain perfluorosulfonic acid ionomer." *Int. J. Hydrogen Energy*, **39**, 11690 (2014).
47. T. H. Mourey, L. A. Slater, R. C. Galipo, and R. J. Koestner, "Size-exclusion chromatography of perfluorosulfonated ionomers." *J. Chromatogr. A*, **1218**, 5801 (2011).
48. R. Koestner, Y. Roiter, I. Kozhinova, and S. Minko, "AFM imaging of adsorbed nafion polymer on mica and graphite at molecular level." *Langmuir*, **27**, 10157 (2011).
49. A. Kusoglu, T. J. Dursch, and A. Z. Weber, "Nanostructure/swelling relationships of bulk and thin-film PFSA ionomers." *Adv. Funct. Mater.*, **26**, 4961 (2016).
50. R. Makharia, M. F. Mathias, and D. R. Baker, "Measurement of catalyst layer electrolyte resistance in PEFCs using electrochemical impedance spectroscopy." *J. Electrochem. Soc.*, **152**, A970 (2005).
51. D. R. Baker, D. A. Caulk, K. C. Neyerlin, and M. W. Murphy, "Measurement of oxygen transport resistance in PEM fuel cells by limiting current methods." *J. Electrochem. Soc.*, **156**, B991 (2009).
52. J. P. Owejan, J. E. Owejan, and W. Gu, "Impact of platinum loading and catalyst layer structure on PEMFC performance." *J. Electrochem. Soc.*, **160**, F824 (2013).
53. Y. Liu, C. Ji, W. Gu, J. Jorne, and H. A. Gasteiger, "Effects of catalyst carbon support on proton conduction and cathode performance in PEM fuel cells." *J. Electrochem. Soc.*, **158**, B614 (2011).
54. W. Gu, D. R. Baker, Y. Liu, and H. A. Gasteiger, "Proton exchange membrane fuel cell (PEMFC) down-the-channel performance model." *Handbook of Fuel Cells*. (John Wiley & Sons, Ltd., New Jersey, United States of America) (2010).
55. B. Loppinet, G. Gebel, and C. E. Williams, "Small-angle scattering study of perfluorosulfonated ionomer solutions." *J. Phys. Chem. B*, **101**, 1884 (1997).
56. G. Gebel, "Structural evolution of water swollen perfluorosulfonated ionomers from dry membrane to solution." *Polymer (Guildf.)*, **41**, 5829 (2000).
57. S. Jiang, K. Q. Xia, and G. Xu, "Effect of additives on self-assembling behavior of nafion in Aqueous media." *Macromolecules*, **34**, 7783 (2001).
58. B. Loppinet and G. Gebel, "Rodlike colloidal structure of short pendant chain perfluorinated ionomer solutions." *Langmuir*, **14**, 1977 (1998).
59. K. D. Kreuer, M. Schuster, B. Obliers, O. Diat, U. Traub, A. Fuchs, U. Klock, S. J. Paddison, and J. Maier, "Short-side-chain proton conducting perfluorosulfonic acid ionomers: why they perform better in PEM fuel cells." *J. Power Sources*, **178**, 499 (2008).
60. N. J. Economou, J. R. O'Dea, T. B. McConaughy, and S. K. Buratto, "Morphological differences in short side chain and long side chain perfluorosulfonic acid proton exchange membranes at low and high water contents." *RSC Adv.*, **3**, 19525 (2013).
61. N. H. Jalani and R. Datta, "The effect of equivalent weight, temperature, cationic forms, sorbates, and nanoinorganic additives on the sorption behavior of Nafion." *J. Memb. Sci.*, **264**, 167 (2005).
62. R. Shimizu, Y.-C. Park, K. Kakinuma, A. Iiyama, and M. Uchida, "Effects of both oxygen permeability and ion exchange capacity for cathode ionomers on the performance and durability of polymer electrolyte fuel cells." *J. Electrochem. Soc.*, **165**, F3063 (2018).
63. S. Poojary, M. N. Islam, U. N. Shrivastava, E. P. L. Roberts, and K. Karan, "Transport and electrochemical interface properties of ionomers in Low-Pt loading catalyst layers: effect of ionomer equivalent weight and relative humidity." *Molecules*, **25**, 3387 (2020).
64. P. J. Dudenas and A. Kusoglu, "Evolution of ionomer morphology from dispersion to film: an in situ X-ray study." *Macromolecules*, **52**, 7779 (2019).
65. Y. Ono, A. Ohma, K. Shinohara, and K. Fushinobu, "Influence of equivalent weight of ionomer on local oxygen transport resistance in cathode catalyst layers." *J. Electrochem. Soc.*, **160**, F779 (2013).
66. M. F. Serincan, U. Pasaogullari, and T. Molter, "Modeling the cation transport in an operating polymer electrolyte fuel cell (PEFC)." *Int. J. Hydrogen Energy*, **35**, 5539 (2010).